batteries

MDPI

Article

Nanostructured Lead Electrodes with Reduced Graphene Oxide for High-Performance Lead–Acid Batteries

Matteo Rossini [1,2], Fabrizio Ganci [1,3], Claudio Zanca [1], Bernardo Patella [1], Giuseppe Aiello [1] and Rosalinda Inguanta [1,*]

[1] Laboratorio di Chimica Fisica Applicata, Dipartimento di Ingegneria, Università di Palermo, Viale delle Scienze, 90128 Palermo, Italy
[2] Applied Electrochemistry, Department of Chemical Engineering, KTH Royal Institute of Technology, SE-100 44 Stockholm, Sweden
[3] Corpo Nazionale dei Vigili del Fuoco, Piazza Viminale 1, 00184 Rome, Italy
* Correspondence: rosalinda.inguanta@unipa.it

Abstract: Nanostructured Pb electrodes consisting of nanowire arrays were obtained by electrodeposition, to be used as negative electrodes for lead–acid batteries. Reduced graphene oxide was added to improve their performances. This was achieved via the electrochemical reduction of graphene oxide directly on the surface of nanowire arrays. The electrodes with and without reduced graphene oxide were tested in a 5 M sulfuric acid solution using a commercial pasted positive plate and an absorbed glass mat separator in a zero-gap configuration. The electrodes were tested in deep cycling conditions with a very low cut-off potential. Charge–discharge tests were performed at 5C. The electrode with reduced graphene oxide outperformed the electrode without reduced graphene oxide, as it was able to work with a very high utilization of active mass and efficiency. A specific capacity of 258 $mAhg^{-1}$–very close to the theoretical one–was achieved, and the electrode lasted for more than 1000 cycles. On the other hand, the electrode without reduced graphene oxide achieved a capacity close to 230 $mAhg^{-1}$, which corresponds to a 90% of utilization of active mass.

Keywords: lead–acid batteries; negative electrode; nanostructures; reduced graphene oxide; template electrodeposition; high C-rate

check for updates

Citation: Rossini, M.; Ganci, F.; Zanca, C.; Patella, B.; Aiello, G.; Inguanta, R. Nanostructured Lead Electrodes with Reduced Graphene Oxide for High-Performance Lead–Acid Batteries. *Batteries* **2022**, *8*, 211. https://doi.org/10.3390/batteries8110211

Academic Editors: Pascal Venet, Karim Zaghib and Seung-Wan Song

Received: 6 September 2022
Accepted: 31 October 2022
Published: 3 November 2022

Publisher's Note: MDPI stays neutral with regard to jurisdictional claims in published maps and institutional affiliations.

Copyright: © 2022 by the authors. Licensee MDPI, Basel, Switzerland. This article is an open access article distributed under the terms and conditions of the Creative Commons Attribution (CC BY) license (https://creativecommons.org/licenses/by/4.0/).

1. Introduction

Even though lead–acid batteries (LABs) are the oldest electrochemical energy storage technology, they still attract some interest due to their low price and easy recyclability [1–3]. On the other hand, they are outperformed by Li-ion batteries (LIBs) when it comes to weight, since their specific energy is limited to 30–40 $Whkg^{-1}$ [4,5], while LIBs can be manufactured with a specific energy up to 250 $Whkg^{-1}$ [6]. LABs also suffer from a cycle life limited to 500 cycles, which dramatically drops when they are operated at a partial state of charge [7–10]. These poor performances, in conjunction with the fact that LABs can operate at a maximum rate of C/5, drastically limit their application in hybrid electrical vehicles and even in renewable energies applications [1,11–15]. The growth of large lead sulfate crystals with low conductivity and low solubility was proven to cause negative electrode failure in demanding conditions [16,17]; this phenomenon is often cited as "hard sulfation" [18].

In the past 30 years, different solutions (such as lighter grid materials, additives for pastes and/or electrolytes, bipolar plates, and gelled electrolytes) have been tested to improve LABs performances [4,19–23]. However, the best solution proposed to date concerns the use of carbon additives for negative plates [24–26]. These additives have proven to suppress hard sulfation [16,27]. Carbon-based electrodes for hybrid devices have also been developed [28,29].

Thin-film and nanostructured PbO_2 electrodes have been synthesized to overcome the limitations of positive pasted plates, increasing active surface and utilization of the active mass [30–37]. For nanostructured PbO_2, even applications for asymmetric supercapacitors have been proposed [38–42]. In past years, the template electrosynthesis technique [43–45] was used by our group to develop free-standing PbO_2 nanowires (NWs) electrodes, which exhibited impressive results in terms of the utilization of active mass and life in deep-cycling conditions, even at 10C [46]. The same results were obtained when we used a similar technique to obtain Pb NWs electrodes [47,48] and in the case of a complete nanostructured battery [49]. In general, the nanostructured morphology allows an improvement of the performances in the electrochemical devices, thanks to the high surface area that guarantees a high number of active sites for the redox reactions [50–54].

Graphene oxide (GO) has attracted our interest as an additive for nanostructured Pb electrodes due to some good results obtained with nanostructured carbon additive for LABs [29,55–58], but also because interesting GO experimental applications in electrochemical storage have been reported [59,60]. Its special properties have made it useful for multiple applications [61–63]. GO structure consists of a few micrometers of large graphene foil, which are decorated by polar oxygen groups such as alcohol and epoxide groups [64]. GO, which is hydrophilic and easy to disperse in water due to its polar groups, is synthetized from natural graphite [65]. Graphite is first oxidized (Hummer's method) and then exfoliated in water by sonication or stirring [66]. Once it is reduced, GO yields the deposition of a graphene-like material—the so-called reduced graphene oxide (rGO). Even though rGO performs less than graphene, as regards conductivity and toughness, for instance [67], this new material can be easily mass produced [68]. In recent years, graphene [55,69,70] and multi-walled carbon nanotubes (MWNT) [55,71] were also tested as additives for the negative electrodes. Furthermore, some attempts were made to exploit GO in the LABs electrode. Yang et al. proposed composite additives with GO and polypyrrole [72] and with GO and PbO [73]. GO doped with N also has potential for application in this field [74]. On the other hand, rGO was added to the negative electrodes as a three-dimensional porous material [75], or as support for TiO_2 nanoparticles [76] and PbO nanoparticles [77].

In this work, we deposited rGO onto our nanostructured Pb electrodes via electrochemical reduction—a simple, economic, and eco-friendly process [68]—to enhance their conductivity and activity. The composite electrodes were tested in a 5 M sulfuric acid solution in a zero-gap configuration using a commercial pasted positive plate and an Absorbed Glass Mat (AGM) separator (Figure 1). Very severe test conditions were adopted to stress the composite electrode. In particular, charge–discharge tests were performed at 5C and a cut-off potential of −0.12 V vs. Mercury Sulphate Electrode (MSE) was imposed, corresponding to a deep discharge, in order to check the lifetime of nanostructured composite electrode in very severe discharge conditions. To underline the effect of rGO, as-prepared electrode without rGO was tested in the same conditions.

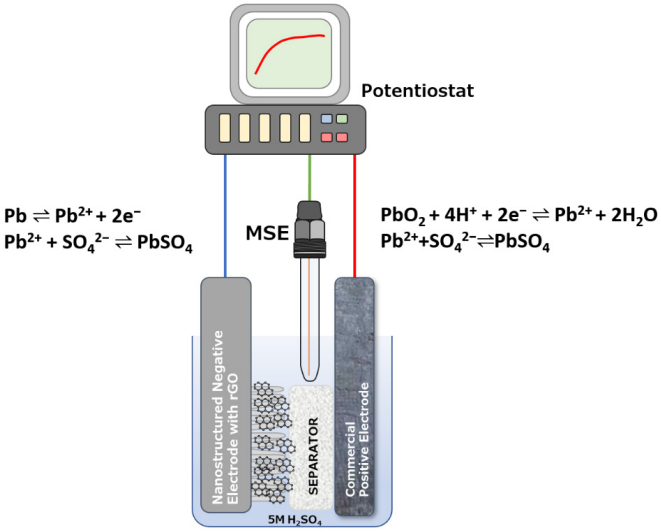

Figure 1. Scheme of nanostructured electrode and battery configuration.

2. Results and Discussion

The morphology of the samples was evaluated by scanning electron microscopy (SEM). The SEM analysis proved that NWs deposition was achieved, as in our previous works [47] (Figure 2A,B). A layer of ordered Pb NWs was present on the surface of the Pb current collector, which was also obtained by electrodeposition.

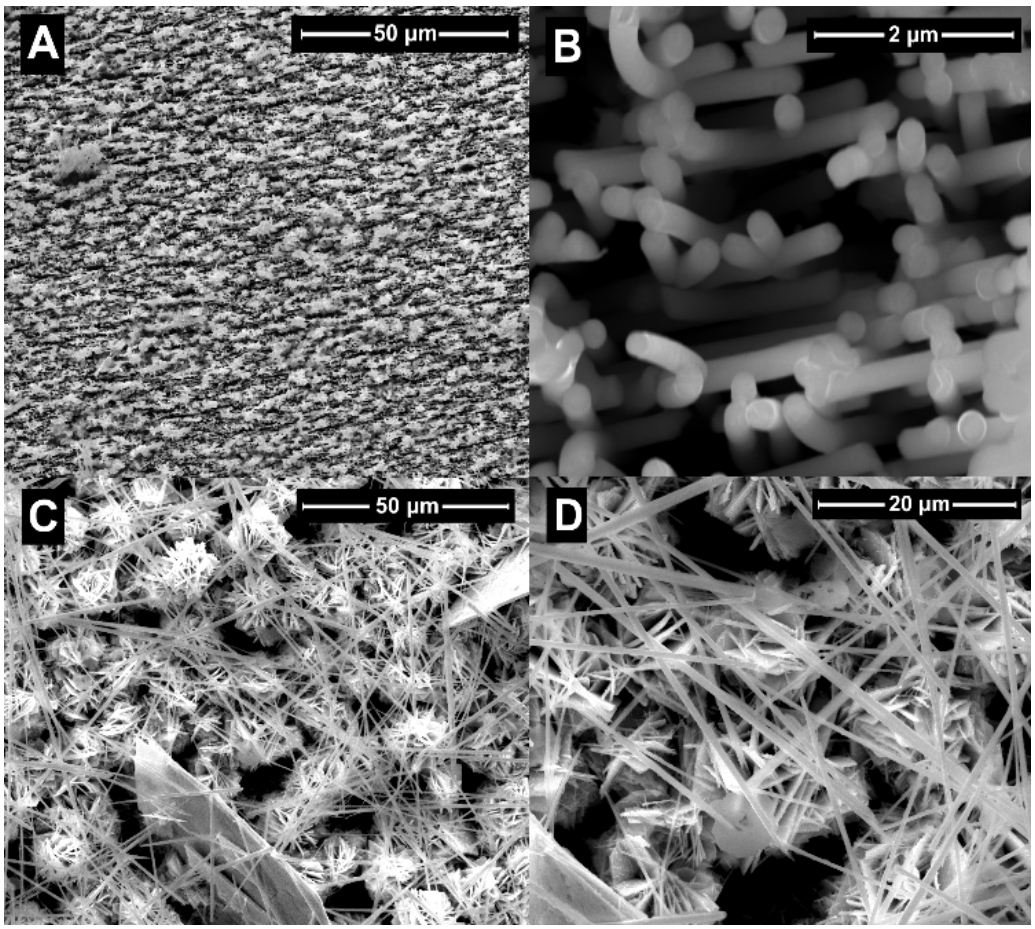

Figure 2. SEM images of lead NWs before (**A**,**B**) and after the deposition of GO (**C**,**D**).

The Pb NWs electrodes were immersed in the solution containing GO (GO dispersion in acetate buffer solution (ABS), pH 5.4) to deposit the rGO on their surface. The electrochemical reduction of GO to rGO occurs following the reaction (1) proposed by Dong et al. [78], which is the most commonly accepted mechanism:

$$GO + xH^+ + ye^- \rightarrow rGO + zH_2O \quad (1)$$

A morphology change happened during the deposition of rGO. The NWs layer disappeared and flower-shaped crystals were present on the surface of the samples (Figure 2C,D). These larger crystals may have formed via oxidation, dissolution of the NWs, and re-precipitation due to the higher solubility of Pb^{2+} in the acetate buffer. Due to their low thickness, the rGO sheets in the SEM images of Figure 2C,D are not clear visible. Despite the change in surface morphology, the electrodes were further tested, since a rearrangement of nanostructures was also recorded in our previous studies, while the electrodes were cycled in sulfuric acid [47]. Furthermore, this new morphology with its flower-shaped structures seemed to offer a high porosity and high surface.

To prove the presence of rGO, further characterizations were performed. In particular, the Raman spectra of the samples were recorded to check the presence of rGO on its surface (Figure 3A). The bands of this spectrum, which are at 87.2, 142.6 and 287.9 cm^{-1}, can be attributed to β-PbO. This attribution was performed using the database [79]. Moreover, the X-ray diffraction (XRD, Figure 3B) shows that its surface mostly comprises β-PbO [80]. Traces of Pb are also revealed. Furthermore, the peak at 386.0 cm^{-1} of Raman shift and one of the peaks of the XRD pattern can be attributed to α-PbO [81]. PbO formation is probably due to air and water exposure. Despite the presence of high-intensity bands at low Raman shift, this spectrum could also reveal some bands with a lower intensity at a higher Raman shift (Figure 3A). In particular, the Raman modes at 1354 and 1598 cm^{-1} were isolated, showing clear evidence of the presence of rGO on the surface of the electrode (see inset of Figure 3A). In Figure 2C, the spectrum of the energy-dispersive X-ray spectroscopy (EDS) of the sample after rGO deposition is reported. Apart from the peaks of Pb, the peaks of C and O are also present.

Composite electrodes were assembled and tested in a zero-gap configuration. For comparison, electrodes without rGO were also tested. Figure 4 summarizes these results. When the nanostructured electrodes were tested in a battery configuration, the electrode without rGO seemed to have a slightly higher performance than during the first 100 cycles. As shown in Figure 4A, its potential is maintained at −1.0 V during the discharge, and it sharply drops afterwards with a rectangular shape curve. On the other hand, the electrode with rGO did not complete most of the charge with a quasi-constant potential during cycle 50 and 100, and it continued to deliver part of the charge after the first knee. However, the electrode with rGO completed the charge at a lower potential and its capacity increased from cycle 100, as also shown in Figure 5. Furthermore, both the electrodes showed a marked performance improvement during these first cycles (Figure 5), as in our previous work [47], with increasingly higher capacity and lower average potential during charge. This behavior is a characteristic of the lead–acid battery and, as reported in [34], was due to the change of the active material morphology. This change in morphology leads to a change in the active material wettability, which increases during the first 100 cycles and then remains stable, as demonstrated in our previous work by a contact angle test. As soon as NWs' wettability increases, the charge drained on discharge increases. In this initial phase, the presence of rGO does not influence the electrode performances, which are governed by the morphology change, and, therefore, in terms of wettability.

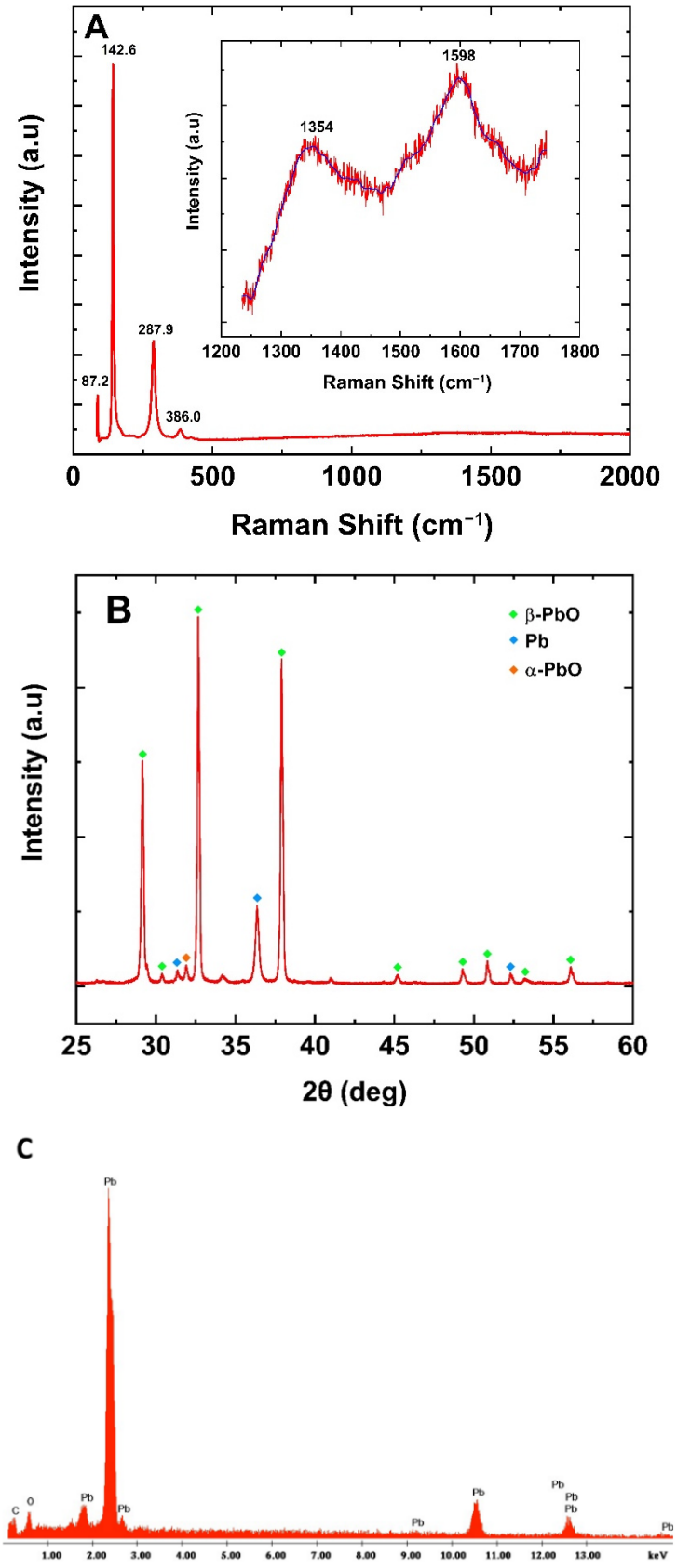

Figure 3. (**A**) Raman spectrum, (**B**) XRD pattern, and (**C**) EDS spectrum of the electrode surface after the deposition of rGO.

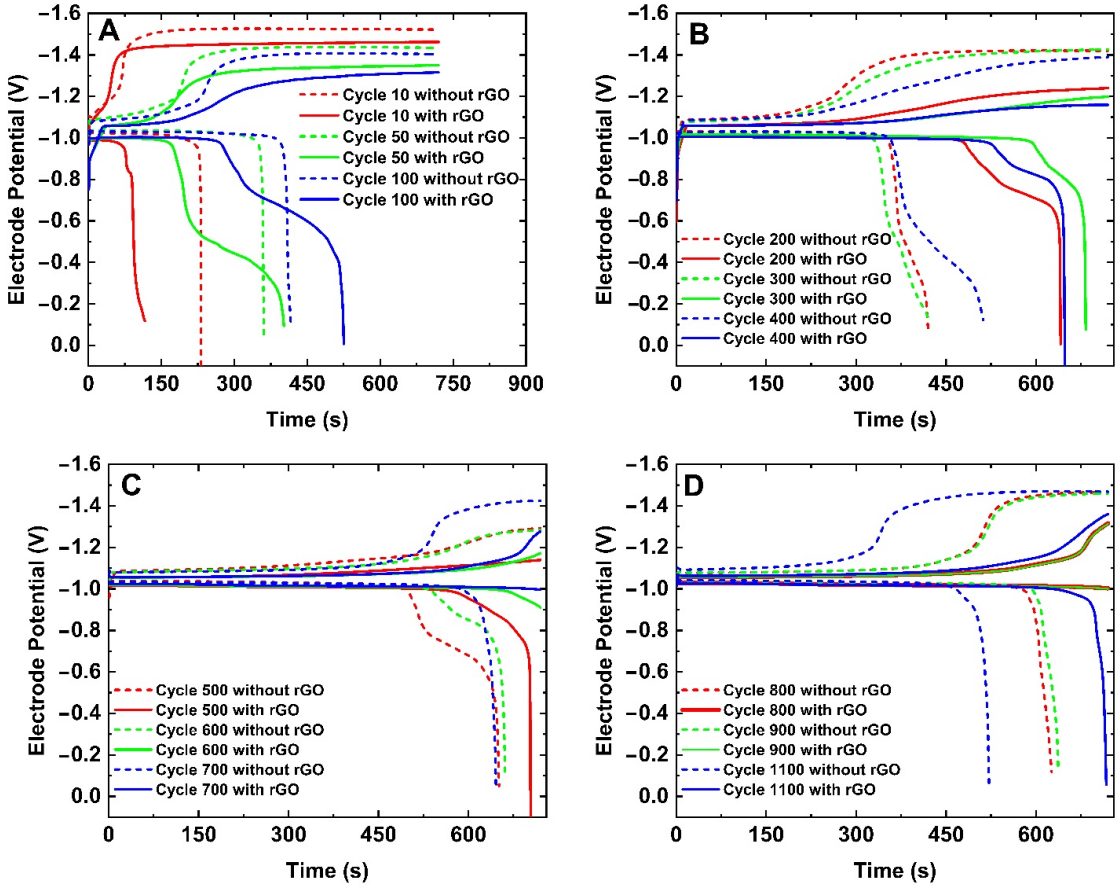

Figure 4. Charge and discharge curve for the nanostructured electrode with rGO and the nanostructured electrode without rGO in 5 M H_2SO_4 (Potential vs. MSE): (**A**) charge-discharge curves from 10th to 100th cycle; (**B**) charge-discharge curves from 200th to 400th cycle; (**C**) charge-discharge curves from 500th to 700th cycle; (**D**) charge-discharge curves from 800th to 1100th cycle.

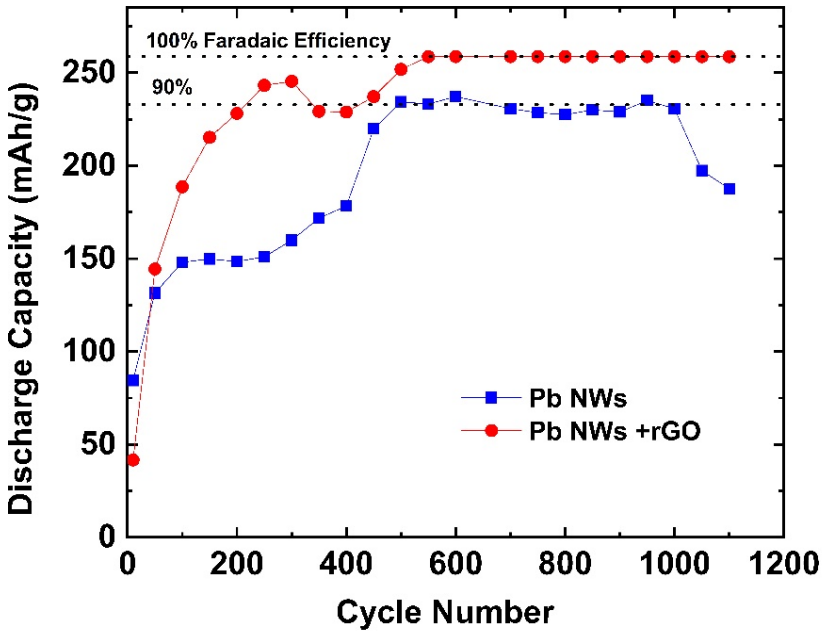

Figure 5. Electrode capacity as a function of cycle number for the nanostructured electrode with rGO and the nanostructured electrode without rGO in 5 M H_2SO_4.

The rGO becomes fundamental in subsequent cycles when the electrode reaches a more or less stable morphology because its presence guarantees a good conductivity of the electrode, and, therefore, a greater conversion efficiency into $PbSO_4$ and vice versa during cycling [75]. Further cycling leads the electrode with rGO to outperform the electrode without rGO (Figures 4B and 5). In particular, its discharged capacity was close to 220 $mAhg^{-1}$ and its faradaic efficiency close to 90%, while the other electrode showed much lower values. In addition, the electrode with rGO completed its charging at −1.2 V and 200 mV below the electrode without rGO.

From cycle 500, both the electrodes showed an important performance improvement (Figures 3C and 5). The electrode without rGO reached the performances which had been met by the electrode with rGO in the previous cycles. Despite this improvement, the electrode with rGO continued to outperform the other electrode. It worked close to the theoretical specific capacity of 258.7 $mAhg^{-1}$, meaning that almost all the mass of the NWs reacts, and close to a unitary faradaic efficiency delivering current at the almost constant voltage of −1.0 V. It also charged at a slightly lower potential. After cycle 900 (Figures 4D and 5), a dramatic performance decay affected the electrode without rGO. Its faradaic efficiency dropped to 70% with a specific capacity lower than 200 $mAhg^{-1}$. Furthermore, this performance decay came after an increase in charging potential during cycles 800–900. As a result, the electrode completed most of the charging at −1.4 V during the last cycles. On the other hand, the electrode with rGO did not face any performance decay, except for the presence of a knee in its discharging curve at cycle 1100 and a slightly higher potential during charge.

The performance improvement is due to the addition of rGO and it can be attributed to the influence of carbon materials on lead electrodes [16,28]. rGO might provide higher conductivity to electrodes when it is fully discharged, suppressing the insulating effect of $PbSO_4$ [17]. This could explain the lower voltage required for charging. Furthermore, the higher capacity and lower potential drop during discharging can be attributable to this effect. In addition, rGO could help in reducing the formation of larger $PbSO_4$ crystals, as carbon additives do, due to its conductivity. This may explain the longer life of the electrode with rGO, since the electrode without rGO probably failed for hard sulphation. However, the presence of an extra active surface does not cause a higher hydrogen evolution rate, as may happen with higher carbon additive loading [6,7,16,28]. In fact, no adverse effect on the faradaic efficiency is reported. Furthermore, carbon additives are also believed to mechanically suppress the formation of larger $PbSO_4$ crystals [16]. Therefore, further work is needed to understand the mechanism of influence of rGO.

3. Materials and Methods

Pb nanostructured electrodes were fabricated as described in our previous work [47]. Pb NWs were obtained via template electrodeposition. The template was a Whatman Cyclopore 47 track-etched polycarbonate membrane (mean pore diameter of 200 nm and 15 µm thick). First, the membrane was gold-sputtered on one side to make its surface electrically conductive. The gold film was 20–30 nm thick. Then, a 30 µm Pb compact current collector was electrodeposited on this surface. This deposition was conducted in three identical steps of 960 s each, using a pulsed current. After each step, the deposition bath (lignin sulfonate 4.5 gL^{-1}, H_3BO_3 15 gL^{-1}, HBF_4 35.2 gL^{-1}, $Pb(BF_4)_2$ 40.5 gL^{-1}) was refreshed. The pulsed current shape was rectangular with a maximum current of -10 $mAcm^{-2}$, lasting for 5 s, and a minimum current of 1 $mAcm^{-2}$, lasting for 0.25 s. A Pt mesh was used as a counter-electrode. The electrodeposition was performed using the Solartron 1470E potentiostat. After deposition, the sample was washed with distilled water, dried, and weighted with an analytical microbalance (Sartorius, mod. Premium Microbalance ME36S). NWs deposition was performed on the other side of the membrane, and NWs were deposited with the same conditions of the current collector. NWs deposition lasted for 450 s to allow the growth of 10 µm-thick nanostructures, as elucidated by our previous work [47]. The sample was again washed, dried, and weighted to estimate the

electrode capacity with the weight of the nanostructures (gravimetric capacity). This is the difference between the weight of the sample after NWs deposition and that before. Membrane dissolution was accomplished in pure dichloromethane with 4 steps lasting 300 s each. For each step, a fresh solvent was used.

The electrode was then sealed in a parafilm and Teflon mask and electric contact was provided with a lead foil. Potentiostatic deposition of rGO was performed in a cylindrical cell (quick fit) with 30 mL of a GO dispersion in acetate buffer solution, pH 5.4 (ABS). The electrode was already sealed in the mask, while the GO concentration was 0.2 gL^{-1}, and Pt-mesh and a saturated SCE served as a counter and reference electrode, respectively. Deposition lasted for 600 s and the electrode potential was maintained at −0.8 V vs. SCE.

SEM (FEG-ESEM, FEI QUANTA 200), Raman (Renishaw, inVia Raman 158 Microscope), and EDS (EDAX Ametek) spectroscopy were carried out in different areas of the electrode. The samples were also characterized by X-ray diffraction (XRD, RIGAKU D-MAX 25600 HK). All characterization methods are detailed in [46,47].

The samples were tested as battery negative electrodes in 5 M of H_2SO_4, using a commercial pasted plate as a positive electrode and AGM separator in a zero-gap configuration. A mercury sulfate electrode (MSE) was added to the set up. Constant current charge–discharge tests were performed at 5C and a cut-off potential of −0.12 V vs. MSE was used.

The first charge of each battery was conducted stepwise, as reported in [47], to avoid severe gas evolution and crack of the electrode. The current was stepwise increased from C/5 to 5C, and each step delivered the same charge.

4. Conclusions

This work pointed out the beneficial influence of rGO on nanostructured Pb electrodes. High-performance nanostructured and rGO additive electrodes were manufactured. First, Pb NWs electrodes were successfully electrodeposited and rGO electrodeposited on their surface. The electrodes were tested under very stressful conditions, in terms of both charge–discharge rate and discharge potential. Despite these conditions, excellent performances were obtained. In fact, the electrodes can work close to the theoretical utilization of active mass and to the capacity of 258.7 $mAhg^{-1}$ with almost unitary faradaic efficiency. Furthermore, the electrode discharges at almost constant potential when a constant current is applied. These better performances are attributed to the high conductivity of rGO, which suppress the activity loss due to the growth of $PbSO_4$ crystals. Further work is needed to understand the exact influence mechanism of rGO, and if it can deliver improved performance at a higher C rate or to Pb electrodes with a different design.

Author Contributions: Conceptualization, M.R. and F.G.; methodology, M.R.; validation, M.R., F.G. and B.P.; formal analysis, M.R. and C.Z.; investigation, M.R., F.G. and B.P.; resources, G.A. and R.I.; data curation, M.R., C.Z. and F.G.; writing—original draft preparation, M.R. and F.G.; writing—review and editing, G.A., B.P., C.Z. and R.I.; supervision, G.A. and R.I.; project administration, G.A. and R.I.; funding acquisition, G.A. and R.I. All authors have read and agreed to the published version of the manuscript.

Funding: This research was funded by the University of Palermo and MIUR, grant number POC01_11121.

Informed Consent Statement: Not applicable.

Data Availability Statement: Not applicable.

Conflicts of Interest: The authors declare no conflict of interest.

References

1. Pavlov, D. *Invention and Development of the Lead–Acid Battery, Lead-Acid Batteries: Science and Technology*; Elsevier: Amsterdam, The Netherlands, 2017; pp. 3–32. [CrossRef]
2. May, G.J.; Davidson, A.; Monahov, B. Lead batteries for utility energy storage: A review. *J. Energy Storage* **2018**, *15*, 145–157. [CrossRef]
3. Vignarooban, K.; Chu, X.; Chimatapu, K.; Ganeshram, P.; Pollat, S.; Johnson, N.G.; Razdan, A.; Pelley, D.S.; Kannan, A.M. State of health determination of sealed lead acid batteries under various operating conditions. *Sustain. Energy Technol. Assess.* **2018**, *18*, 134–139. [CrossRef]
4. Linden, D.; Beard, K.W.; Reddy, T.B. (Eds.) *Linden's Handbook of Batteries*, 5th ed.; McGraw-Hill: New York, NY, USA, 2019.
5. Castro, M.T.; del Rosario, J.A.D.; Chong, M.N.; Chuang, P.-Y.A.; Lee, J.; Ocon, J.D. Multiphysics modeling of lithium-ion, lead-acid, and vanadium redox flow batteries. *J. Energy Storage* **2021**, *42*, 102982. [CrossRef]
6. Zubi, G.; Dufo-López, R.; Carvalho, M.; Pasaoglu, G. The lithium-ion battery: State of the art and future perspectives. *Renew. Sustain. Energy Rev.* **2018**, *89*, 292–308. [CrossRef]
7. Garche, J. (Ed.) *Encyclopedia of Electrochemical Power Sources*; Elsevier: Amsterdam, The Netherlands; Academic Press: Amsterdam, The Netherlands, 2009.
8. Ibrahim, N.S.M.; Ponniran, A.; Rahman, R.A.; Martin, M.P.; Yassin, A.; Eahambram, A.; Aziz, M.H. Parameters observation of restoration capacity of industrial lead acid battery using high current pulses. *Int. J. Power Electron. Drive Syst.* **2020**, *11*, 1596. [CrossRef]
9. Kim, S.J.; Co, L.S.E.; Seo, S.W.; An, S.Y.; Kim, B.-G.; Son, J.H.; Gil Jung, Y. Charging-Discharging Behavior and Performance of AGM Lead Acid Battery/EDLC Module for x-HEV. *Korean J. Mater. Res.* **2021**, *31*, 84–91. [CrossRef]
10. Zhang, W.-L.; Yin, J.; Lin, Z.-Q.; Shi, J.; Wang, C.; Liu, D.-B.; Wang, Y.; Bao, J.-P.; Lin, H.-B. Lead-carbon electrode designed for renewable energy storage with superior performance in partial state of charge operation. *J. Power Sources* **2017**, *342*, 183–191. [CrossRef]
11. Fatullah, M.A.; Rahardjo, A.; Husnayain, F. Analysis of Discharge Rate and Ambient Temperature Effects on Lead Acid Battery Capacity. In Proceedings of the 2019 IEEE International Conference on Innovative Research and Development (ICIRD), Jakarta, Indonesia, 28–30 June 2019; pp. 1–5. [CrossRef]
12. Blecua, M.; Fatas, E.; Ocon, P.; Valenciano, J.; de la Fuente, F.; Trinidad, F. Influences of carbon materials and lignosulfonates in the negative active material of lead-acid batteries for microhybrid vehicles. *J. Energy Storage* **2017**, *11*, 55–63. [CrossRef]
13. Deveau, J.; White, C.; Swan, L.G. Lead-acid battery response to various formation levels—Part A: Recommended formation levels for off-grid solar and conventional applications. *Sustain. Energy Technol. Assess.* **2015**, *11*, 1–10. [CrossRef]
14. Yin, J.; Lin, N.; Lin, Z.; Wang, Y.; Chen, C.; Shi, J.; Bao, J.; Lin, H.; Feng, S.; Zhang, W. Hierarchical porous carbon@PbO1-x composite for high-performance lead-carbon battery towards renewable energy storage. *Energy* **2019**, *193*, 116675. [CrossRef]
15. Fernández, M.; Valenciano, J.; Trinidad, F.; Muñoz, N. The Use of Activated Carbon and Graphite for the Development of Lead-Acid Batteries for Hybrid Vehicle Applications. *J. Power Sources* **2010**, *195*, 4458–4469. [CrossRef]
16. Pavlov, D. *Lead-Acid Batteries—Science and Technology—A Handbook of Lead-Acid Battery Technology and Its Influence on the Product*, 2nd ed.; Elsevier: Amsterdam, The Netherlands, 2017.
17. Yang, F.; Zhou, H.; Hu, J.; Ji, S.; Lai, C.; Wang, H.; Sun, J.; Lei, L. Thorn-like and dendrite lead sulfate as negative electrode materials for enhancing the cycle performance of lead-acid batteries. *J. Energy Storage* **2022**, *49*, 104112. [CrossRef]
18. Tao, S.; Fan, H.; Lei, Y.; Xu, X.; Sun, Y.; You, B.; Gao, Y. The proactive maintenance for the irreversible sulfation in lead-based energy storage systems with a novel resonance method. *J. Energy Storage* **2021**, *42*, 103093. [CrossRef]
19. Chen, Z.; Li, J.; Yu, J.; Wu, L.; Zhou, S.; Rao, Y.; Cao, J. The critical role of aluminum sulfate as electrolyte additive on the electrochemical performance of lead-acid battery. *Electrochim. Acta* **2022**, *407*, 139877. [CrossRef]
20. Binh, P.T.; van Anh, N.T.; Thuy, M.T.T.; Xuan, M.T.; Duyen, N.T. Electrochemical study on the structure of PbO2 in mixed gel electrolytes during cycling by cyclic voltammetry. *Vietnam J. Chem.* **2021**, *59*, 767–774. [CrossRef]
21. Yin, J.; Lin, N.; Zhang, W.; Lin, Z.; Zhang, Z.; Wang, Y.; Shi, J.; Bao, J.; Lin, H. Highly reversible lead-carbon battery anode with lead grafting on the carbon surface. *J. Energy Chem.* **2018**, *27*, 1674–1683. [CrossRef]
22. Van Anh, N.T.; Thuy, M.T.T.; Xuan, M.T.; Binh, P.T. Study on electrochemical properties of gelled electrolytes using nano fumed silica in the presence of some organic additives. *Int. J. Nanotechnol.* **2020**, *17*, 648. [CrossRef]
23. Lim, T.S.; Kim, S.J.; Kim, S.D.; Yang, S.C.; Jung, Y.-G. Performance Characteristics of Lead Acid Battery with the Contents of Sodium Perborate Tetrahydrate (SPT) in Positive Plate Active Material. *Korean J. Mater. Res.* **2020**, *30*, 426–434. [CrossRef]
24. Zhang, W.; Yin, J.; Lin, H.; Lu, K.; Feng, F.; Qiu, X. Design principles of lead-carbon additives toward better lead-carbon batteries. *Curr. Opin. Electrochem.* **2021**, *30*, 426–434. [CrossRef]
25. Blecua, M.; Fatas, E.; Ocon, P.; Gonzalo, B.; Merino, C.; de la Fuente, F.; Valenciano, J.; Trinidad, F. Graphitized Carbon Nanofibers: New additive for the Negative Active Material of Lead Acid Batteries. *Electrochim. Acta* **2017**, *257*, 109–117. [CrossRef]
26. Yin, J.; Zhang, W.; Sun, G.; Xiao, S.; Lin, H. Oxygen-functionalized defect engineering of carbon additives enable lead-carbon batteries with high cycling stability. *J. Energy Storage* **2021**, *43*, 103205. [CrossRef]
27. Sawai, K.; Funato, T.; Watanabe, M.; Wada, H.; Nakamura, K.; Shiomi, M.; Osumi, S. Development of additives in negative active-material to suppress sulfation during high-rate partial-state-of-charge operation of lead–acid batteries. *J. Power Sources* **2006**, *158*, 1084–1090. [CrossRef]

28. Garche, J.; Karden, E.; Moseley, P.T.; Rand, D.A.J. (Eds.) *Lead-Acid Batteries for Future Automobiles*; Elsevier: Amsterdam, The Netherlands, 2017.
29. Yin, J.; Lin, H.; Shi, J.; Lin, Z.; Bao, J.; Wang, Y.; Lin, X.; Qin, Y.; Qiu, X.; Zhang, W. Lead-Carbon Batteries toward Future Energy Storage: From Mechanism and Materials to Applications. *Electrochem. Energy Rev.* **2022**, *5*, 1–32. [CrossRef]
30. Morales, J.; Petkova, G.; Cruz, M.; Caballero, A. Nanostructured Lead Dioxide Thin Electrode. *Electrochem. Solid-State Lett.* **2004**, *7*, A75–A77. [CrossRef]
31. Ghasemi, S.; Mousavi, M.F.; Karami, H.; Shamsipur, M.; Kazemi, S. Energy storage capacity investigation of pulsed current formed nano-structured lead dioxide. *Electrochim. Acta* **2006**, *52*, 1596–1602. [CrossRef]
32. Bervas, M.; Perrin, M.; Geniès, S.; Mattera, F. Low-cost synthesis and utilization in mini-tubular electrodes of nano PbO_2. *J. Power Sources* **2007**, *173*, 570–577. [CrossRef]
33. Perret, P.; Brousse, T.; Bélanger, D.; Guay, D. Electrochemical Template Synthesis of Ordered Lead Dioxide Nanowires. *J. Electrochem. Soc.* **2009**, *156*, A645–A651. [CrossRef]
34. Egan, D.; Low, C.; Walsh, F. Electrodeposited nanostructured lead dioxide as a thin film electrode for a lightweight lead-acid battery. *J. Power Sources* **2011**, *196*, 5725–5730. [CrossRef]
35. Chen, T.; Huang, H.; Ma, H.; Kong, D. Effects of surface morphology of nanostructured PbO_2 thin films on their electrochemical properties. *Electrochim. Acta* **2012**, *88*, 79–85. [CrossRef]
36. Fan, N.; Sun, C.; Kong, D.; Qian, Y. Chemical synthesis of PbO_2 particles with multiple morphologies and phases and their electrochemical performance as the positive active material. *J. Power Sources* **2014**, *254*, 323–328. [CrossRef]
37. Zhao, X. Electrodeposited PbO_2 Thin Films with Different Surface Structure as Positive Plate in Lead Acid Batteries. *Int. J. Electrochem. Sci.* **2018**, 3745–3756. [CrossRef]
38. Li, X.; Li, S.; Ma, X.; Tang, K.; Wang, Z.; Hao, X.; Abudula, A.; Guan, G. Template-free electro-synthesis of PbO_2 nanorod with chrysanthemum-like array. *Mater. Lett.* **2018**, *238*, 85–88. [CrossRef]
39. Yu, N.; Gao, L.; Zhao, S.; Wang, Z. Electrodeposited PbO_2 thin film as positive electrode in PbO_2/AC hybrid capacitor. *Electrochim. Acta* **2009**, *54*, 3835–3841. [CrossRef]
40. Zhang, W.; Lin, H.; Kong, H.; Lu, H.; Yang, Z.; Liu, T. Preparation and characterization of lead dioxide electrode with three-dimensional porous titanium substrate for electrochemical energy storage. *Electrochim. Acta* **2014**, *139*, 209–216. [CrossRef]
41. Yao, Y.; Chen, X.; Yu, N.; Wei, F.; Feng, H. Preparation and Supercapacitive Performance of Lead Dioxide Electrodes with Three-Dimensional Porous Structure. *Russ. J. Electrochem.* **2018**, *54*, 585–591. [CrossRef]
42. Yao, Y.; Li, M.; Zhang, X.; Lu, Z.; Wei, F. Influence of manganese content on the supercapacitive performance of PbO_2-MnO_2 electrodes. *Turk. J. Chem.* **2018**, *42*, 472–481. [CrossRef]
43. Li, J.; Sattayasamitsathit, S.; Dong, R.; Gao, W.; Tam, R.; Feng, X.; Ai, S.; Wang, J. Template electrosynthesis of tailored-made helical nanoswimmers. *Nanoscale* **2013**, *6*, 9415–9420. [CrossRef]
44. Patella, B.; Piazza, S.; Sunseri, C.; Inguanta, R. Anodic Alumina Membranes: From Electrochemical Growth to Use as Template for Fabrication of Nanostructured Electrodes. *Appl. Sci.* **2022**, *12*, 869. [CrossRef]
45. Lai, M.; Riley, J. Templated electrosynthesis of nanomaterials and porous structures. *J. Colloid Interface Sci.* **2008**, *323*, 203–212. [CrossRef]
46. Inguanta, R.; Vergottini, F.; Ferrara, G.; Piazza, S.; Sunseri, C. Effect of temperature on the growth of α-PbO_2 nanostructures. *Electrochim. Acta* **2010**, *55*, 8556–8562. [CrossRef]
47. Insinga, M.G.; Oliveri, R.L.; Sunseri, C.; Inguanta, R. Template electrodeposition and characterization of nanostructured Pb as a negative electrode for lead-acid battery. *J. Power Sources* **2018**, *413*, 107–116. [CrossRef]
48. Inguanta, R.; Rinaldo, E.; Piazza, S.; Sunseri, C. Lead Nanowires for Microaccumulators Obtained Through Indirect Electrochemical Template Deposition. *Electrochem. Solid-State Lett.* **2010**, *13*, K1–K4. [CrossRef]
49. Oliveri, R.; Insinga, M.; Pisana, S.; Patella, B.; Aiello, G.; Inguanta, R. High-Performance Lead-Acid Batteries Enabled by Pb and PbO_2 Nanostructured Electrodes: Effect of Operating Temperature. *Appl. Sci.* **2021**, *11*, 6357. [CrossRef]
50. Wang, J.; Li, Z.; Gu, Z. A comprehensive review of template-synthesized multi-component nanowires: From interfacial design to sensing and actuation applications. *Sens. Actuators Rep.* **2021**, *3*, 100029. [CrossRef]
51. Inguanta, R.; Piazza, S.; Sunseri, C.; Cino, A.; di Dio, V.; Cascia, D.L.; Miceli, R.; Rando, C.; Zizzo, G. *An Electrochemical Route Towards the Fabrication of Nanostructured Semiconductor Solar Cells, SPEEDAM 2010*; IEEE: Pisa, Italy, 2010; pp. 1166–1171. [CrossRef]
52. Kelaidis, N.; Zervos, M.; Lathiotakis, N.N.; Chroneos, A.; Tanasă, E.; Vasile, E. Vapor–liquid–solid growth and properties of one dimensional PbO and PbO/SnO_2 nanowires. *Mater. Adv.* **2021**, *3*, 1695–1702. [CrossRef]
53. Battaglia, M.; Inguanta, R.; Piazza, S.; Sunseri, C. Fabrication and characterization of nanostructured Ni–IrO2 electrodes for water electrolysis. *Int. J. Hydrog. Energy* **2014**, *39*, 16797–16805. [CrossRef]
54. Madusanka, S.A.U.A.; Mahadiulwewa, D.M.O.R.; Samarakoon, S.P.A.A.J.; Sandeepanie, K.A.H.; Damayanthi, R.M.T. Improving the Performance of Lead Acid Batteries using Nano-Technology. In Proceedings of the Moratuwa Engineering Research Conference (MERCon), Moratuwa, Sri Lanka, 27–30 July 2019; pp. 589–593. [CrossRef]
55. Logeshkumar, S.; Manoharan, R. Influence of some nanostructured materials additives on the performance of lead acid battery negative electrodes. *Electrochim. Acta* **2014**, *144*, 147–153. [CrossRef]
56. Lach, J.; Wróbel, K.; Wróbel, J.; Podsadni, P.; Czerwiński, A. Applications of carbon in lead-acid batteries: A review. *J. Solid State Electrochem.* **2019**, *23*, 693–705. [CrossRef]

57. Blecua, M.; Romero, A.; Ocon, P.; Fatas, E.; Valenciano, J.; Trinidad, F. Improvement of the lead acid battery performance by the addition of graphitized carbon nanofibers together with a mix of organic expanders in the negative active material. *J. Energy Storage* **2019**, *23*, 106–115. [CrossRef]
58. Arun, S.; Kiran, K.U.V.; Mayavan, S. Effects of carbon surface area and morphology on performance of stationary lead acid battery. *J. Energy Storage* **2020**, *32*, 101763. [CrossRef]
59. Tian, Y.; Yu, Z.; Cao, L.; Zhang, X.L.; Sun, C.; Wang, D.-W. Graphene oxide: An emerging electromaterial for energy storage and conversion. *J. Energy Chem.* **2020**, *55*, 323–344. [CrossRef]
60. Berbeć, S.; Żołądek, S.; Jabłońska, A.; Palys, B. Electrochemically reduced graphene oxide on gold nanoparticles modified with a polyoxomolybdate film. Highly sensitive non-enzymatic electrochemical detection of H_2O_2. *Sens. Actuators B Chem.* **2018**, *258*, 745–756. [CrossRef]
61. Nong, J.; Lan, G.; Jin, W.; Luo, P.; Guo, C.; Tang, X.; Zang, Z.; Wei, W. Eco-friendly and high-performance photoelectrochemical anode based on $AgInS_2$ quantum dots embedded in 3D graphene nanowalls. *J. Mater. Chem. C* **2019**, *7*, 9830–9839. [CrossRef]
62. Liu, X.; Xu, T.; Li, Y.; Zang, Z.; Peng, X.; Wei, H.; Zha, W.; Wang, F. Enhanced X-ray photon response in solution-synthesized $CsPbBr_3$ nanoparticles wrapped by reduced graphene oxide. *Sol. Energy Mater. Sol. Cells* **2018**, *187*, 249–254. [CrossRef]
63. Wei, J.; Zang, Z.; Zhang, Y.; Wang, M.; Du, J.; Tang, X. Enhanced performance of light-controlled conductive switching in hybrid cuprous oxide/reduced graphene oxide (Cu_2O/rGO) nanocomposites. *Opt. Lett.* **2017**, *42*, 911–914. [CrossRef] [PubMed]
64. He, H.; Klinowski, J.; Forster, M.; Lerf, A. A new structural model for graphite oxide. *Chem. Phys. Lett.* **1998**, *287*, 53–56. [CrossRef]
65. Alam, S.N.; Sharma, N.; Kumar, L. Synthesis of Graphene Oxide (GO) by Modified Hummers Method and Its Thermal Reduction to Obtain Reduced Graphene Oxide (rGO)*. *Graphene* **2017**, *6*, 1–18. [CrossRef]
66. Zhu, Y.; Murali, S.; Cai, W.; Li, X.; Suk, J.W.; Potts, J.R.; Ruoff, R.S. Graphene and Graphene Oxide: Synthesis, Properties, and Applications. *Adv. Mater.* **2010**, *22*, 3906–3924. [CrossRef]
67. Pei, S.; Cheng, H.-M. The reduction of graphene oxide. *Carbon* **2012**, *50*, 3210–3228. [CrossRef]
68. Toh, S.Y.; Loh, K.S.; Kamarudin, S.K.; Daud, W.R.W. Graphene production via electrochemical reduction of graphene oxide: Synthesis and characterization. *Chem. Eng. J.* **2014**, *251*, 422–434. [CrossRef]
69. Yeung, K.K.; Zhang, X.; Kwok, S.C.T.; Ciucci, F.; Yuen, M.M.F. Enhanced cycle life of lead-acid battery using graphene as a sulfation suppression additive in negative active material. *RSC Adv.* **2015**, *5*, 71314–71321. [CrossRef]
70. Chang, S.-H.; Kung, K.-C.; Huang, W.-C.; Liu, W.-R. Few-layer graphene as an additive in negative electrodes for lead-acid batteries. *Thin Solid Film.* **2022**, *753*, 139273. [CrossRef]
71. Li, J.; Cao, J.; Chen, Z.; Yu, J.; Zhang, J.; Chen, B.; Wu, L.; Zhou, S.; Rao, Y. Improving the performance of recovered lead oxide powder from waste lead paste as active material for lead-acid battery. *Int. J. Energy Res.* **2022**, *46*, 14268–14282. [CrossRef]
72. Yang, H.; Qiu, Y.; Guo, X. Effects of PPy, GO and PPy/GO composites on the negative plate and on the high-rate partial-state-of-charge performance of lead-acid batteries. *Electrochim. Acta* **2016**, *215*, 346–356. [CrossRef]
73. Yang, H.; Qi, K.; Gong, L.; Liu, W.; Zaman, S.; Guo, X.; Qiu, Y.; Xia, B.Y. Lead Oxide Enveloped in N-Doped Graphene Oxide Composites for Enhanced High-Rate Partial-State-of-Charge Performance of Lead-Acid Battery. *ACS Sustain. Chem. Eng.* **2018**, *6*, 11408–11413. [CrossRef]
74. Wang, X.-R.; Zhong, J.; Zhu, K.-D.; Wang, S.-L. Nitrogen-doped redox graphene as a negative electrode additive for lead-acid batteries. *J. Energy Storage* **2021**, *44*, 103454. [CrossRef]
75. Long, Q.; Ma, G.; Xu, Q.; Ma, C.; Nan, J.; Li, A.; Chen, H. Improving the cycle life of lead-acid batteries using three-dimensional reduced graphene oxide under the high-rate partial-state-of-charge condition. *J. Power Sources* **2017**, *343*, 188–196. [CrossRef]
76. Vangapally, N.; Jindal, S.; Gaffoor, S.; Martha, S.K. Titanium dioxide-reduced graphene oxide hybrid as negative electrode additive for high performance lead-acid batteries. *J. Energy Storage* **2018**, *20*, 204–212. [CrossRef]
77. Tao, D.; Liu, X.; Li, Z.; Yang, H.; Wang, J.; Zhang, Q. PbO nanoparticles anchored on reduced graphene oxide for enhanced cycle life of lead-carbon battery. *Electrochim. Acta* **2022**, *432*, 141228. [CrossRef]
78. Zhou, M.; Wang, Y.; Zhai, Y.; Zhai, J.; Ren, W.; Wang, F.; Dong, S. Controlled Synthesis of Large-Area and Patterned Electrochemically Reduced Graphene Oxide Films. *Chem. A Eur. J.* **2009**, *15*, 6116–6120. [CrossRef]
79. Lafuente, B.; Downs, R.T.; Yang, H.; Stone, N. The power of databases: The RRUFF project. In *Highlights in Mineralogical Crystallography*; Armbruster, T., Danisi, R.M., Eds.; De Gruyter: Berlin, Germany, 2015; pp. 1–30. [CrossRef]
80. Wang, Y.; Lin, X.; Zhang, H.; Wen, T.; Huang, F.; Li, G.; Wang, Y.; Liao, F.; Lin, J. Selected-control hydrothermal growths of α- and β-PbO crystals and orientated pressure-induced phase transition. *CrystEngComm* **2012**, *15*, 3513–3516. [CrossRef]
81. Güngör, A.; Genç, R.; Özdemir, T. Facile Synthesis of Semiconducting Nanosized 0d and 2d Lead Oxides Using a Modified Co-Precipitation Method. *J. Turk. Chem. Soc. Sect. A Chem.* **2017**, *4*, 1017–1030. [CrossRef]